Supplemental material for
"Nonreciprocal single-photon band structure"

Jiang-Shan Tang,[1,2] Wei Nie,[3] Lei Tang,[1] Mingyuan Chen,[1]
Xin Su,[1,4] Yanqing Lu,[1,2] Franco Nori,[3,5] and Keyu Xia[1,2,6,7*]
[1] *College of Engineering and Applied Sciences, National Laboratory of Solid State Microstructures, and Collaborative Innovation Center of Advanced Microstructures, Nanjing University, Nanjing 210023, China*
[2] *School of Physics, Nanjing University, Nanjing 210023, China*
[3] *RIKEN Quantum Computing Center, RIKEN Cluster for Pioneering Research, Wako-shi, Saitama 351-0198, Japan*
[4] *School of Electronic Science and Engineering, Nanjing University, Nanjing 210023, China*
[5] *Physics Department, The University of Michigan, Ann Arbor, Michigan 48109-1040, USA*
[6] *Jiangsu Key Laboratory of Artificial Functional Materials, Nanjing University, Nanjing 210023, China*
[7] *Key Laboratory of Intelligent Optical Sensing and Manipulation (Nanjing University), Ministry of Education, Nanjing 210023, China*

In this supplemental material, we derive the recursive boundary Green function, the Zak phase of Hamiltonian, and provide a detailed derivation of the transfer matrix method. We show that the property of non-reciprocal single-photon edge states in our system can be used to realize a single-photon circulator. Then, we exhibit that the single-photon transmission is immune to the backscattering in the non-reciprocal single-photon band gap, and discuss the effects of the on-site disorder and the number of unit cells on our chiral QE-CROW system. Finally, we perform a first-principles simulation of our frequency-multiplexed single-photon circulator using the finite-difference time-domain method.

CONTENTS

I. Recursive boundary Green function of the system 1
II. Zak's winding phase and chiral symmetry of Hamiltonian 3
III. The transfer matrix formalism of our chiral QE-CROW system 5
IV. Tunneling enabled single-photon circulator 8
V. The effect of the scatterer 9
VI. The maximal on-site disorder 11
VII. Influence of the number of unit cells 13
VIII. First-principle analysis using FDTD method 14
References 16

I. RECURSIVE BOUNDARY GREEN FUNCTION OF THE SYSTEM

Here, we study the localization properties of edge states and their relationship with the coupling strengths, $\{g, J_1, J_2\}$, when our system is excited in the $\mathrm{CW}_A - \mathrm{CCW}_B$ supermode (forward input). In this case, our QE-CROW system is equivalent to an L-type trimer chain with each unit cell containing three sites, the QE, the A-sublattice resonator, and the B-sublattice resonator. The QE is only coupled with the A-sublattice resonator. We divide the unit cell into A and B sublattice groups, where the A sublattice contains the A-sublattice resonator and the QE, and the B sublattice only involves the B-sublattice resonator. Therefore, this L-type trimer chain can be treated as an SSH-like model. We use the recursive boundary Green function method to link the existence of edge states with the fixed points of the recursion [1, 2]. Hereafter, we consider the case $J_1 < J_2$, which corresponds to the situation with edge states. In contrast, there are no edge states in the opposite case, i.e., $J_1 \geq J_2$.

Following the calculation steps in Ref. [1], we can relate the boundary Green function G_N of this SSH-like chain with N unit cells to the boundary Green function G_{N-1} of a chain with $(N-1)$ unit cells and write the Dyson equation:

$$\left(\epsilon_N^{-1} - V_{N-1} G_{N-1} V_{N-1}^{\dagger}\right) G_N = \mathbb{I}\,, \tag{S1}$$

where $\epsilon_N^{-1} = \mathbb{I}\omega - h_N$ is the bare Green function of the Nth unit cell and V_{N-1} is correlated with coupling strengths $\{g, J_1, J_2\}$. To prove that our system has edge states located at the left boundary of the chain, we consider the left boundary Green function and obtain

$$\epsilon_n^{-1} = \begin{cases} \mathbb{I}\omega & n = 2N-1 \\ \begin{pmatrix} \omega & -g \\ -g & \omega \end{pmatrix} & n = 2N \end{cases}, \qquad V_n = \begin{cases} \begin{pmatrix} 0 \\ J_1 \end{pmatrix} & n = 2N-1 \\ J_2 & n = 2N \end{cases} \tag{S2}$$

from Eq. (1) in the main text. By iterating the recursion Eq. (S1) from the left boundary, we can obtain a recursion for the $2N$th and the $(2N-1)$th cells,

$$\left[\begin{pmatrix} \omega & -g \\ -g & \omega \end{pmatrix} - \begin{pmatrix} 0 \\ J_1 \end{pmatrix} G_{2N-1}^{L} \begin{pmatrix} 0 & J_1 \end{pmatrix}\right] G_{2N}^{L} = \mathbb{I}\,, \tag{S3a}$$

$$\left[\begin{pmatrix} \omega & 0 \\ 0 & \omega \end{pmatrix} - J_2^2 G_{2N-2}^{L}\right] G_{2N-1}^{L} = \mathbb{I}\,, \tag{S3b}$$

respectively. Here, G_{2N}^L and G_{2N-2}^L take the form of a 2×2 matrix,

$$G_{2N}^{L} = \begin{pmatrix} G_{11}^{2N} & G_{12}^{2N} \\ G_{21}^{2N} & G_{22}^{2N} \end{pmatrix}, \quad G_{2N-2}^{L} = \begin{pmatrix} G_{11}^{2N-2} & G_{12}^{2N-2} \\ G_{21}^{2N-2} & G_{22}^{2N-2} \end{pmatrix}. \tag{S4}$$

Substituting Eq. (S4) into Eqs. (S3), we obtain

$$\left(\omega - J_2^2 G_{11}^{2N-2}\right) G_{2N-1}^{L} = 1\,, \tag{S5a}$$

$$G_{11}^{2N}\left(\omega^2 - \omega J_1^2 G_{2N-1}^{L} - g^2\right) - \left(\omega - J_1^2 G_{2N-1}^{L}\right) = 0\,. \tag{S5b}$$

Then we have

$$G_{11}^{2N} = \frac{\omega\left(\omega - J_2^2 G_{11}^{2N-2}\right) - J_1^2}{\left(\omega^2 - g^2\right)\left(\omega - J_2^2 G_{11}^{2N-2}\right) - J_1^2\omega}\,. \tag{S6}$$

In order to analyze the recursion, we further write it as

$$G_{11}^{2N} - G_{11}^{2N-2} = \xi_L\left(G_{11}^{2N-2}\right), \tag{S7}$$

where the function $\xi_L(x)$ is defined as

$$\xi_L(x) = \frac{\omega\left(\omega - J_2^2 x\right) - J_1^2}{\left(\omega^2 - g^2\right)\left(\omega - J_2^2 x\right) - J_1^2\omega} - x. \tag{S8}$$

The fixed-point boundary Green functions can be obtained by solving the zeros of the function $\xi_L(x)$. We can write the solution for Eq. S8 as follows:

$$x = \frac{\omega(\omega^2 - g^2 + J_2^2 - J_1^2) \pm \sqrt{\omega^2(\omega^2 - g^2 + J_2^2 - J_1^2)^2 - 4J_2^2(\omega^2 - g^2)(\omega^2 - J_1^2)}}{2J_2^2(\omega^2 - g^2)}\,, \tag{S9}$$

and expand in power series of $(\omega \pm g)$,

$$G_{\text{reg}}^{L} = \pm\frac{J_1^2 - 4g^2 - J_2^2}{8gJ_2^2} + O(\omega \pm g), \tag{S10}$$

$$G^{L}_{\rm sing} = \frac{J_2^2 - J_1^2}{2J_2^2\left(\omega \pm g\right)} \pm \frac{J_1^2 - 4g^2 - J_2^2}{8gJ_2^2} + O(\omega \pm g). \tag{S11}$$

The above fixed-point boundary Green functions characterize the absence and presence of edge states localized on the left boundary of the chain. Corresponding to the edge state, the band-gap state makes the boundary Green function singular for $\omega \pm g$, see Eq. (S11). In contrast, when the boundary Green function is regular [corresponding to Eq. (S10)], there are no edge states. Further, when $\xi_L^{'}(x) < 0$, it holds a stable fixed point, thus we have

$$\left.\frac{\partial \xi_L\left(G^{L}_{\rm sing}\right)}{\partial x}\right|_{\omega=\pm g} = \frac{J_1^2}{J_2^2} - 1 < 0. \tag{S12}$$

We can find that only when $|J_1| < |J_2|$, the fixed point is stable, which means that there are edge states localized at the left boundary of the chain.

Similarly, when we consider the right boundary Green function, we have:

$$\epsilon_n^{-1} = \begin{cases} \begin{pmatrix} \omega & -g \\ -g & \omega \end{pmatrix} & n = 2N-1 \\ \mathbb{I}\omega & n = 2N \end{cases}, \qquad V_n = \begin{cases} \begin{pmatrix} J_1 & 0 \end{pmatrix} & n = 2N-1 \\ J_2 & n = 2N \end{cases}. \tag{S13}$$

With the same calculation procedure, we can derive the iterative relation:

$$G^{R}_{2N} = \left\{\omega - J_1^2\left[\left(\omega - J_2^2 G^{R}_{2N-2}\right)^2 - g^2\right]^{-1}\right\}^{-1}. \tag{S14}$$

We now rewrite the recursion Eq. (S14) as

$$G^{R}_{2N} - G^{R}_{2N-2} = \xi_R(G^{R}_{2N-2}), \tag{S15}$$

with

$$\xi_R(x) = \left\{\omega - J_1^2\left[\left(\omega - J_2^2 x\right)^2 - g^2\right]^{-1}\right\}^{-1} - x. \tag{S16}$$

The fixed-point boundary Green function can be obtained by seeking the zeros of Eq. (S16), that is

$$\omega J_2^4 x^3 - \left(2\omega^2 J_2^2 + J_2^4\right)x^2 + \left[\omega\left(\omega^2 - g^2 + 2J_2^2\right) - J_1^2\right]x + g^2 - \omega^2 = 0. \tag{S17}$$

The singularity of the solution of Eq. (S17) characterizes the existence of edge states. For this cubic equation, using the famous Cardano formula, we can find that a singularity only appears at $\omega = 0$. Therefore, this means that there is a right edge state at zero energy. Indeed, under the condition of $J_1 < J_2$, the presence of edge states at zero energy is a characteristic of this SSH-like chain. Unlike the left edge state, its energy remain unchanged because the B-sublattice resonator is not coupled with the QE.

II. ZAK'S WINDING PHASE AND CHIRAL SYMMETRY OF HAMILTONIAN

In the nontrivial topological case, i.e., $J_1 < J_2$, nonreciprocal single-photon band structures of the chiral QE-CROW system are shown in Fig. 2 in the main text. The bands are well isolated in both forward- and backward-input cases. In the single-excitation space, we can define an Abelian Zak's phase to each band [3, 4]

$$Z_p = i\int_{-\pi}^{\pi} dk \langle \zeta_{k,p}|\partial_k|\zeta_{k,p}\rangle, \tag{S18}$$

where $p = 1, 2, 3$ ($p = 1, 2$) labels the bands in increasing energy for the forward-input case (the backward-input case). The Bloch wave function $\zeta_{k,p}$ is consistent with the main text.

We first consider the backward-input case corresponding to a standard SSH model. The Hamiltonian in wavevector space is

$$H_{\mathrm{CCW}_A-\mathrm{CW}_B}(k)=\begin{pmatrix} 0 & J_1+J_2e^{-ik} \\ J_1+J_2e^{ik} & 0 \end{pmatrix} . \tag{S19}$$

Using the Pauli matrix σ_z, we have $\sigma_z H_{\mathrm{CCW}_A-\mathrm{CW}_B}(k)\sigma_z^{-1}=-H_{\mathrm{CCW}_A-\mathrm{CW}_B}(k)$. Therefore, the system possesses the chiral symmetries in this situation. By diagonalizing Eq. (S19), we obtain

$$|\zeta_{k,1}\rangle=\frac{1}{\sqrt{2}}\begin{pmatrix} -\frac{\sqrt{J_1^2+J_2^2+2J_1J_2\cos(k)}}{J_1+J_2e^{ik}} \\ 1 \end{pmatrix} , \tag{S20a}$$

$$|\zeta_{k,2}\rangle=\frac{1}{\sqrt{2}}\begin{pmatrix} \frac{\sqrt{J_1^2+J_2^2+2J_1J_2\cos(k)}}{J_1+J_2e^{ik}} \\ 1 \end{pmatrix} . \tag{S20b}$$

Substituting Eqs. (S20) into Eq. (S18), we get

$$Z_1=Z_2=\pi\ \mathrm{mod}(2\pi) , \tag{S21}$$

when $J_2=2J_1$. For this SSH model, topological phase transition occurs at $J_2/J_1=1$ [3].

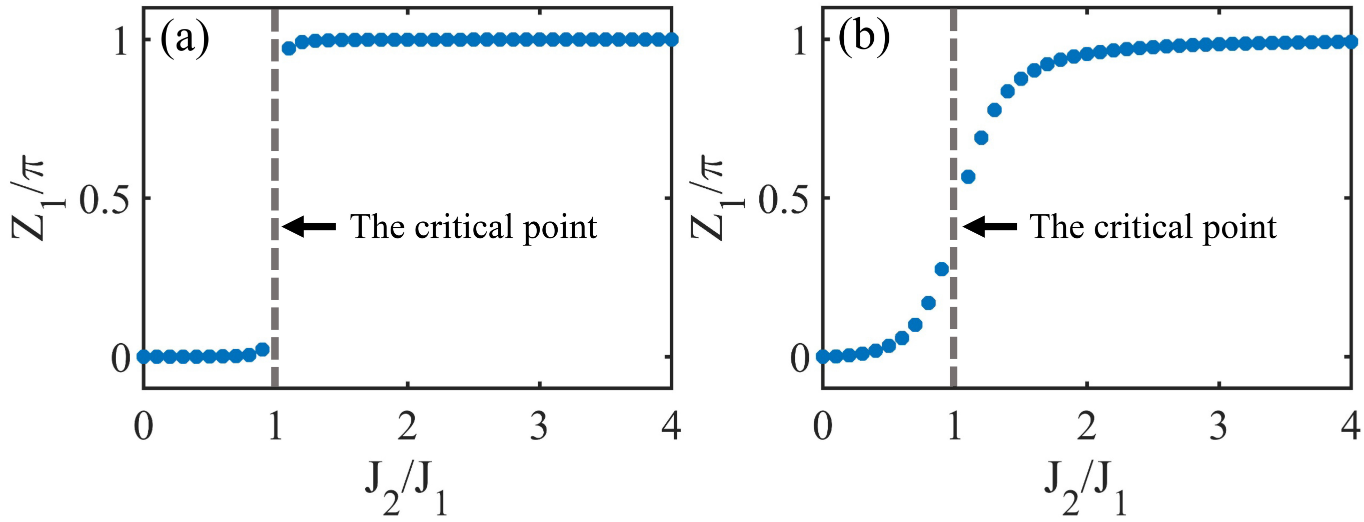

FIG. S1. The Zak phase for the lower band versus J_2/J_1 in different coupling strengthes, $g/\Omega=1\times10^{-5}$ in (a) and $g/\Omega=1\times10^{-4}$ in (b). Other parameters are $J_1/\Omega=3\times10^{-4}$.

Then we discuss the case of the forward input, in which the QEs couple with the A-sublattice resonators to form an L-shaped trimer chain. The Hamiltonian in wavevector space can be written as

$$H_{\mathrm{CW}_A-\mathrm{CCW}_B}(k)=\begin{pmatrix} 0 & g & J_1+J_2e^{-ik} \\ g & 0 & 0 \\ J_1+J_2e^{ik} & 0 & 0 \end{pmatrix} . \tag{S22}$$

By defining a unitary and Hermitian matrix

$$\chi=\begin{pmatrix} -1 & 0 & 0 \\ 0 & 1 & 0 \\ 0 & 0 & 1 \end{pmatrix} , \tag{S23}$$

we find that the Hamiltonian of Eq. (S22) satisfies

$$\chi H_{\mathrm{CW}_A-\mathrm{CCW}_B}\chi^{-1} = -H_{\mathrm{CW}_A-\mathrm{CCW}_B}\ . \tag{S24}$$

Thus, in the forward-input case, the system still preserves the chiral symmetry. By diagonalizing Eq. (S22), we obtain

$$|\zeta_{k,1}\rangle = \frac{\sqrt{J_1^2+J_2^2+2J_1J_2\cos(k)}}{\sqrt{2\left[g^2+J_1^2+J_2^2+2J_1J_2\cos(k)\right]}}\begin{pmatrix} -\frac{\sqrt{g^2+J_1^2+J_2^2+2J_1J_2\cos(k)}}{J_1+J_2e^{ik}} \\ \frac{g}{J_1+J_2e^{ik}} \\ 1 \end{pmatrix}, \tag{S25a}$$

$$|\zeta_{k,2}\rangle = \frac{1}{\sqrt{g^2+J_1^2+J_2^2+2J_1J_2\cos(k)}}\begin{pmatrix} 0 \\ J_1+J_2e^{-ik} \\ g \end{pmatrix}, \tag{S25b}$$

$$|\zeta_{k,3}\rangle = \frac{\sqrt{J_1^2+J_2^2+2J_1J_2\cos(k)}}{\sqrt{2\left[g^2+J_1^2+J_2^2+2J_1J_2\cos(k)\right]}}\begin{pmatrix} \frac{\sqrt{g^2+J_1^2+J_2^2+2J_1J_2\cos(k)}}{J_1+J_2e^{ik}} \\ \frac{g}{J_1+J_2e^{ik}} \\ 1 \end{pmatrix}. \tag{S25c}$$

Using Eqs. (S25) and (S18), we show the Zak phase as a function of J_2/J_1, see Fig. S1. The coupling to QEs breaks the inversion symmetry of the forward-input system. It leads to a change in bulk-band structure of the original SSH model. When the QE-resonator strength is small, such as $g/\Omega = 10^{-5}$, this change is negligible. The Zak phases are still quantized both for the upper and lower bulk bands, see Fig. S1(a). But as g increases, the situation is different. The effect of QE-resonator coupling emerges. The Zak phase of the lower band is no longer quantized, especially in the vicinity of the critical point $J_2 = J_1$, showing a trend of continuous change, see Fig. S1(b). There is no well-defined topological invariant due to the broken-inversion symmetry [2, 5, 6].

Likewise, the original left edge state is also changed because of the coupling of the QEs to the A-sublattice resonator. It becomes doublet, forming two superstates of the A-sublattice resonators and the QEs, with an energy split proportional to the coupling strength g. This change suggests that the left edge states of the L-shaped chain have a topological origin inherited from the SSH model.

III. THE TRANSFER MATRIX FORMALISM OF OUR CHIRAL QE-CROW SYSTEM

We derive the transfer matrix formalism to treat the dynamics of our chiral QE-CROW system. We find that the single-photon dispersion relations solved by the transfer matrix are consistent with the results obtained by solving the Hamiltonian directly in the main text.

Our chiral 1D-CROW system is shown in the main text. Each resonator, with a resonance frequency Ω and an internal dissipation γ_{in}, supports two degenerate optical whispering-gallery modes: clockwise and counterclockwise modes. The adjacent resonators are separated by Λ. The resonators are divided into two groups A and B, where the A-sublattice resonator couples with a two-level QE in a chiral way and the B-sublattice resonator decouples from the QEs. As the light travels in the CROW, the excited propagation modes in the A and B sublattices are opposite, thus forming N unit cells. We assume that QEs couple to the clockwise mode in the A-sublattice resonator, but decouple from the counterclockwise mode.

The chiral QE-light interaction implies that only the clockwise-circulating single photon interacts with the QE and passes through it with a transmission coefficient t_{qe}; but the counterclockwise-circulating single photon decouples from the QE. We can treat the QE in the resonator as a quantum scatterer in an optical waveguide [7]. Then, we obtain t_{qe} by calculating the single-photon transmission in the QE-waveguide system [8],

$$t_{\mathrm{qe}} = \frac{\omega-\omega_q+i(\gamma-\Gamma)}{\omega-\omega_q+i(\gamma+\Gamma)}, \tag{S26}$$

where ω (ω_q) is the central (resonance) frequency of the incident photon (the QE), γ is the dissipation rate of the QE. Γ is the decay rate from the QE into the resonator, and the QE-resonator coupling strength is $g \approx \sqrt{2\Gamma \times \mathcal{F}}$ [7], where the $\mathcal{F}$ is the free spectral range of the resonator.

Note that the chiral QE-light interaction leads to a vanishing reflection of the single-photon propagation [8]. The

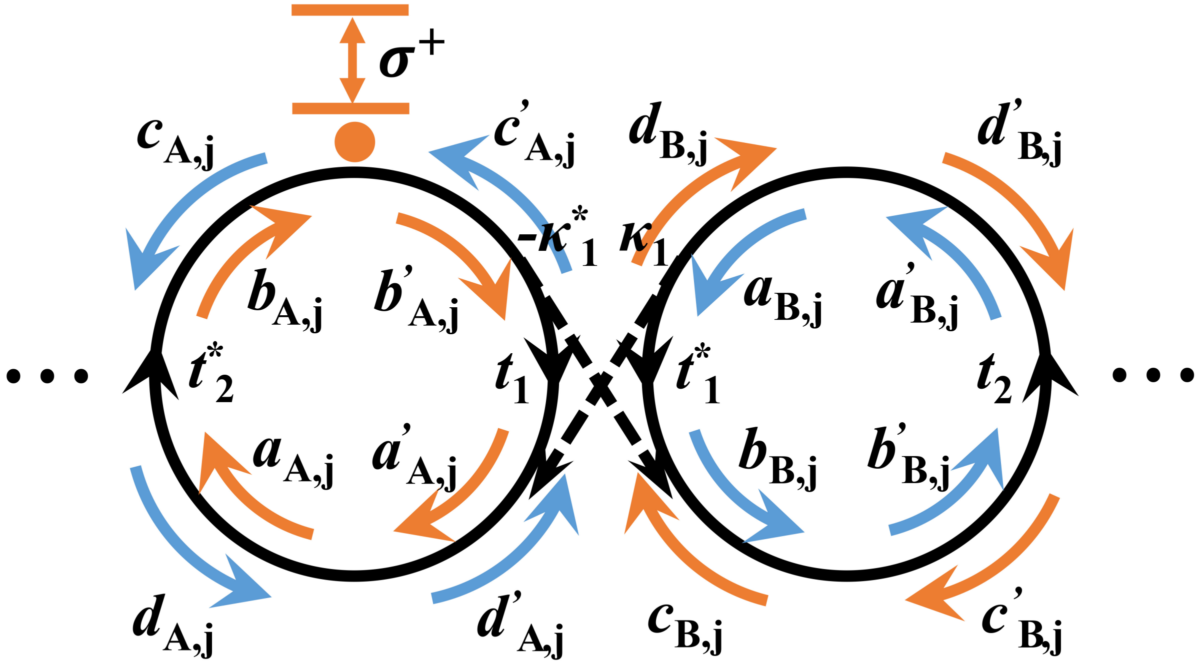

FIG. S2. The unit cell presented in the main text, with the sublattices A and B. The yellow/blue arrows represent the circulating direction of the clockwise/counterclockwise whispering-gallery modes.

QEs can modify the phase and amplitude of the single-photon field propagating along the clockwise direction in the A-sublattice resonators, but do not excite the counterclockwise-circulating field via radiation as a normal achiral system.

Theoretically, the QE chirally coupled to the resonator can be treated as a “single-photon phase-amplitude modulator” [7]. For simplicity, we take $t_{\mathrm{qe}} \equiv \exp(i\varphi)$ ($\varphi = \varphi_1 + i\varphi_2$), where $\varphi_1(\omega) = \arg(t_{\mathrm{qe}})$ and $\exp(-\varphi_2) = |t_{\mathrm{qe}}|$ describe the changes in phase and amplitude, respectively. From Eq. (S26), we have $|t_{\mathrm{qe}}| \approx 1$ and $\varphi_2 \approx 0$ when $\gamma \ll \Gamma$. In this case, the QEs only change the phase φ_1 of the single-photon field of the clockwise mode.

Then, using the notation from Fig. S2, we can write the transfer matrix formalism for the 1D-CROW system:

$$x_{j+1} = P_2 Q_2 P_1 Q_1 x_j. \tag{S27}$$

Here, $x_j = (a_{\mathrm{A,j}}\ b_{\mathrm{A,j}}\ c_{\mathrm{A,j}}\ d_{\mathrm{A,j}})^T$ is a vector of the wave-packet amplitudes. The above matrices $\{P_1, P_2\}$ and $\{Q_1, Q_2\}$ describe inter-sublattice and intra-sublattice transfer, respectively. We refer to $P_{1,2}$ and $Q_{1,2}$ as coupling and propagation matrices, and they can be written as:

$$P_1 = \begin{pmatrix} M_{\mathrm{c},1} & 0 \\ 0 & M_{\mathrm{c},1} \end{pmatrix}, \quad Q_1 = \begin{pmatrix} M_{\mathrm{p,A}} & 0 \\ 0 & M_{\mathrm{p,B}} \end{pmatrix}, \tag{S28a}$$

$$P_2 = \begin{pmatrix} M_{\mathrm{c},2} & 0 \\ 0 & M_{\mathrm{c},2} \end{pmatrix}, \quad Q_2 = \begin{pmatrix} M_{\mathrm{p,B}} & 0 \\ 0 & M_{\mathrm{p,B}} \end{pmatrix}, \tag{S28b}$$

$$M_{\mathrm{c},1} = \frac{1}{\kappa_1}\begin{pmatrix} 1 & -t_1 \\ t_1^* & -1 \end{pmatrix}, \quad M_{\mathrm{c},2} = \frac{1}{\kappa_2}\begin{pmatrix} 1 & -t_2 \\ t_2^* & -1 \end{pmatrix}, \tag{S28c}$$

$$M_{\mathrm{p,A}} = \begin{pmatrix} e^{-i\theta(R)} & 0 \\ 0 & e^{i[\theta(R)+\varphi]} \end{pmatrix}, \quad M_{\mathrm{p,B}} = \begin{pmatrix} e^{-i\theta(R)} & 0 \\ 0 & e^{i\theta(R)} \end{pmatrix}, \tag{S28d}$$

where $\{t_1, t_2\}$ and $\{\kappa_1, \kappa_2\}$ are the transmission and coupling coefficients of the intrasite and intersite resonators. According to waveguide mode coupling theory, $t_{1/2}$ are real, $\kappa_{1/2}$ are imaginary, and $|t_{1/2}|^2 + |\kappa_{1/2}|^2 = 1$. Note that the coupling strengths between resonators can be deduced from $J_{1/2} = \mathrm{Im}\left(\kappa_{1/2}\right) \times \mathcal{F}$ [7]. The factor $\theta(L) = \pi\beta L$ is the propagation phase change dependent on the path L of the light propagating in the resonator, where β is the propagation constant, given by $\beta = n_{\text{eff}}\omega/c$. From Eqs. S28, we can find that the propagation modes in each resonator are decoupled. In other words, the transfer relation of the wave-packet amplitudes are only from (a, b) to $\left(a^{'}, b^{'}\right)$ and from (c, d) to $\left(c^{'}, d^{'}\right)$. Therefore, when we consider one of them, we can study it in the form of a 2×2 matrix as shown in the main text.

Using Bloch's theorem [9, 10], we can obtain the eigenvalue equations of the system under two excitation modes (i.e., the $\text{CW}_A - \text{CCW}_B$ supermode and the $\text{CCW}_A - \text{CW}_B$ supermode),

$$\text{Det}|M_{\text{c},2}M_{\text{p,B}}M_{\text{c},1}M_{\text{p,A}} - \exp(-2iK\Lambda)| = 0, \tag{S29}$$

and

$$\text{Det}|M_{\text{c},2}M_{\text{p,B}}M_{\text{c},1}M_{\text{p,B}} - \exp(-2iK\Lambda)| = 0, \tag{S30}$$

respectively. Above, K is the Bloch quasi-momentum and 2Λ is the unit spacing. Solving the above equations, we have the dispersion relation

$$\cos(2K\Lambda) = \left[\cos(2\theta) - t_1 t_2\right]/\kappa_1\kappa_2 \tag{S31}$$

for the $\text{CCW}_A - \text{CW}_B$ supermode and the dispersion relation

$$\cos\left(2K\Lambda - \frac{\varphi}{2}\right) = \left[\cos\left(2\theta + \frac{\varphi}{2}\right) - t_1 t_2 \cos\left(\frac{\varphi}{2}\right)\right]/\kappa_1\kappa_2 \tag{S32}$$

for the $\text{CW}_A - \text{CCW}_B$ supermode.

Obviously, the dispersion relation of the $\text{CW}_A - \text{CCW}_B$ supermode is different from Eq. (S31). This nonreciprocal single-photon dispersion property occurs because the chiral QE-light coupling breaks the time-reversal symmetry of the system. In the $\text{CW}_A - \text{CCW}_B$ supermode, the QE interacts with the single-photon evanescent field and introduces an additional propagating phase φ to the single-photon field. In contrast, this extra phase factor disappears in the $\text{CCW}_A - \text{CW}_B$ supermode. In the absence of the QEs, we have $\varphi = 0$ and then Eq. (S32) reduces to the reciprocal case Eq. (S31). In this case, the single-photon dispersion in two counter-propagating cases becomes reciprocal.

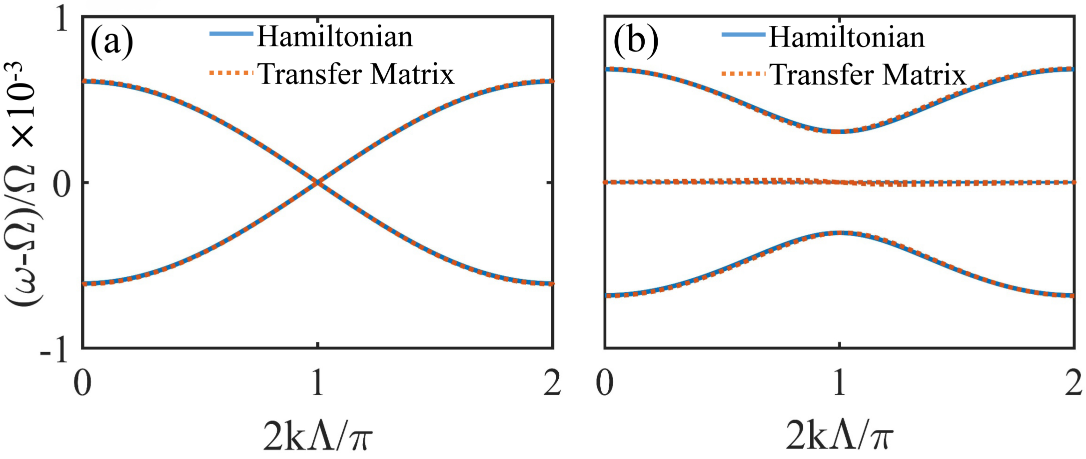

FIG. S3. The single-photon band structures calculated by the Hamiltonian and transfer matrix method, respectively. (a) The system is excited in the $\text{CCW}_A - \text{CW}_B$ supermode and (b) is excited in the $\text{CW}_A - \text{CCW}_B$ supermode. Other parameters are $\Gamma/\Omega = 1.5 \times 10^{-5}$ corresponding to $g/\Omega = 3 \times 10^{-4}$, $\kappa_1 = \kappa_2 = 0.1i$ corresponding to $J_1/\Omega = J_2/\Omega = 3 \times 10^{-4}$, and $\gamma = 0$.

Now we consider a simple example, $\kappa_1 = \kappa_2$, which means that the coupling strengths between resonators are equal, i.e., $J_1 = J_2$. Considering the resonators with a radius of $r = 40$ μm, $\Omega/2\pi = 195$ THz and $n_{\text{eff}} = 2$, we obtain $\mathcal{F}/2\pi = 0.6$ THz. We take $\kappa_1 = \kappa_2 = 0.1i$ and $\Gamma/\Omega = 1.5 \times 10^{-5}$, thus $J_1/\Omega = J_2/\Omega = 3 \times 10^{-4}$ and $g/\Omega = 3 \times 10^{-4}$. These parameter settings are consistent with Fig. 4 in the main text. Figure S3 shows the single-photon band structures of our system under two different excitation modes. The red dotted curves are the dispersion relations corresponding to the real solutions of Eqs. (S31) and (S32). And the blue solid curves are the results of directly solving the eigenequations of the Hamiltonian. It can be found that the results of transfer matrix calculation are consistent with solving the eigenvalues and eigenstates of the Hamiltonian.

IV. TUNNELING ENABLED SINGLE-PHOTON CIRCULATOR

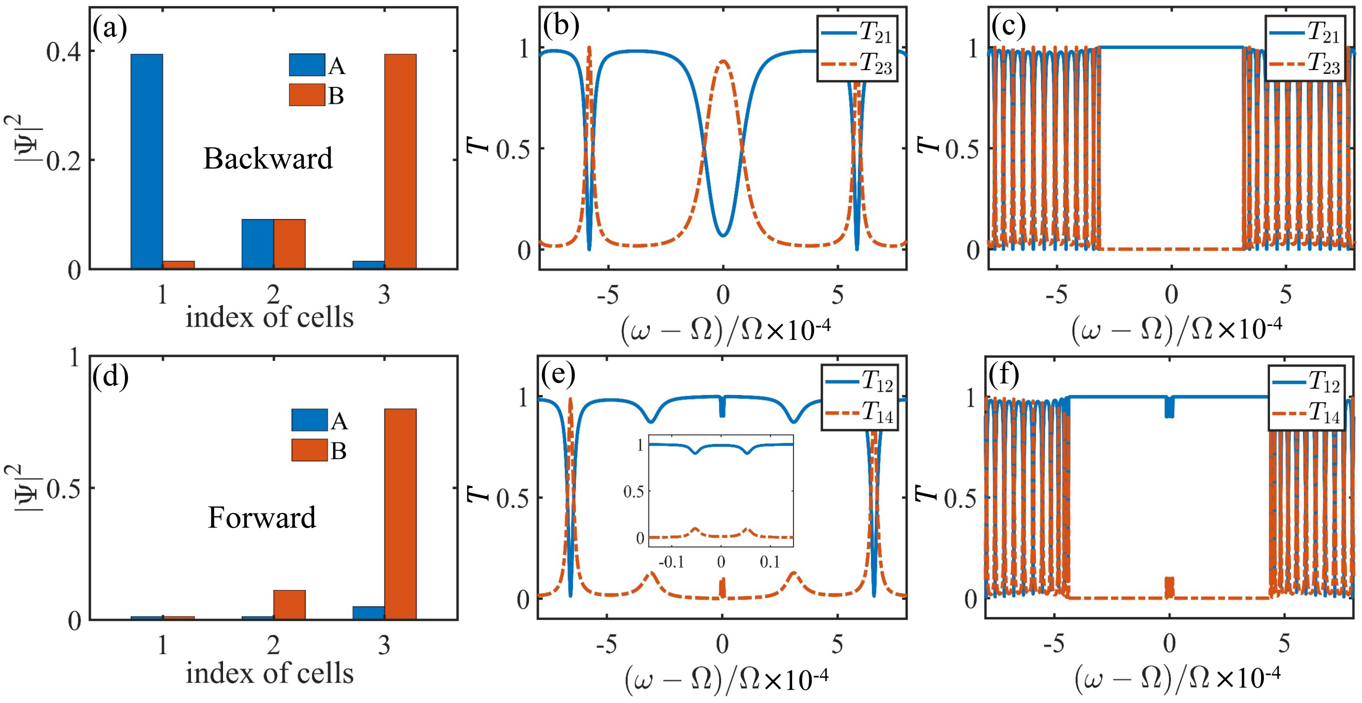

FIG. S4. Nonreciprocal probability distribution and transmission of the chiral QE-CROW system at zero-energy frequency. (a-c) for the backward input without coupling to the QEs, $g = 0$. (d-f) for the forward input with coupling to the QEs, $g/\Omega = 3 \times 10^{-4}$. The number of cells is $N = 3$ in (a, b, d, e) and $N = 20$ in (c, f). Other parameters are $J_1/\Omega = 3 \times 10^{-4}$, $J_2 = 2J_1$.

In this section, we discuss the influence of edge-state tunneling. When a single photon enters port 1 or 3, it excites the $\mathrm{CW}_A - \mathrm{CCW}_B$ supermode of the CROW, which corresponds to the forward input, see Fig. 1 in the main text. The photon incident to ports 2 and 4 (backward input) excites the oppositely propagating mode, i.e., the $\mathrm{CCW}_A - \mathrm{CW}_B$ supermode. We consider the case with edge states, that is $J_1 < J_2$. As the discussion in the main text, the edge states in our chiral QE-CROW system exhibit a nonreciprocal characteristic. This unique property can be used to achieve a single-photon circulator via single-photon edge-state tunneling effect.

In the backward case, the QEs have no interaction with the resonators. The two degenerate zero-energy eigenstates are odd and even superpositions of states localized exponentially on the left and right boundaries. When the number of cells is small, such as $N = 3$, there is an exponentially small overlap between the left and right edges [3], see Fig. S4(a). This leads to a probability that the photon passes through the CROW, that is, an edge-state tunneling. In stark contrast, there is negligible overlap of left and right edge states at the zero-energy frequency, as shown in Fig. S4(d), because of the energy splitting of left edge state. Due to the coupling with the QEs, the left single-photon edge state becomes a doublet with an energy splitting proportional to the coupling strength g, while the energy of the right single-photon edge state is still zero. As a result, this edge-state tunneling effect disappears at the zero-energy frequency in the forward case. Therefore, we can realize a single-photon circulator via the nonreciprocal SPESs with few unit cells.

Figures S4(b) and (e) show the nonreciprocal single-photon transmission at the zero-energy frequency induced by edge-state tunneling in the number of cells $N = 3$. When a single photon is incident to port 2, corresponding to the backward case, the transmission T_{23} can reach about 0.93 because of the edge-state tunneling effect, see Fig. S4(b). But for the forward input, i.e., the single photon entering port 1, the light cannot enter the CROW at all, and thus $T_{14} \approx 0$ ($T_{12} \approx 1$), see Fig. S4(e). Due to the symmetry of the CROW, we have $T_{34} = T_{12}$ and $T_{41} = T_{23}$. As a result, we can construct a single-photon circulator using the edge-state tunneling with a circling photon transport $1 \rightarrow 2 \rightarrow 3 \rightarrow 4 \rightarrow 1$ at the zero-energy frequency. The fidelity and the average photon survival probability of the circulator are calculated as $\{0.96, 0.99\}$. The negligible transmission near the zero energy in the inset of Fig. S4(e) results from the single-photon flat band. The small dips appearing at $(\omega - \Omega) = \pm g$ correspond to the eigenvalue of the left edge states, and their depth decreases with increasing QE-resonator coupling strength g.

When the number of cells becomes large, this edge-state tunneling vanishes for the backward case due to the absence of overlap between the left and right edges. In this case, the single-photon circulator cannot be constructed at zero-energy frequency, see Figs. S4(c) and (f). The slight transmission at zero energy in Fig. S4(f) is caused by the single-photon flat band for the forward input.

V. THE EFFECT OF THE SCATTERER

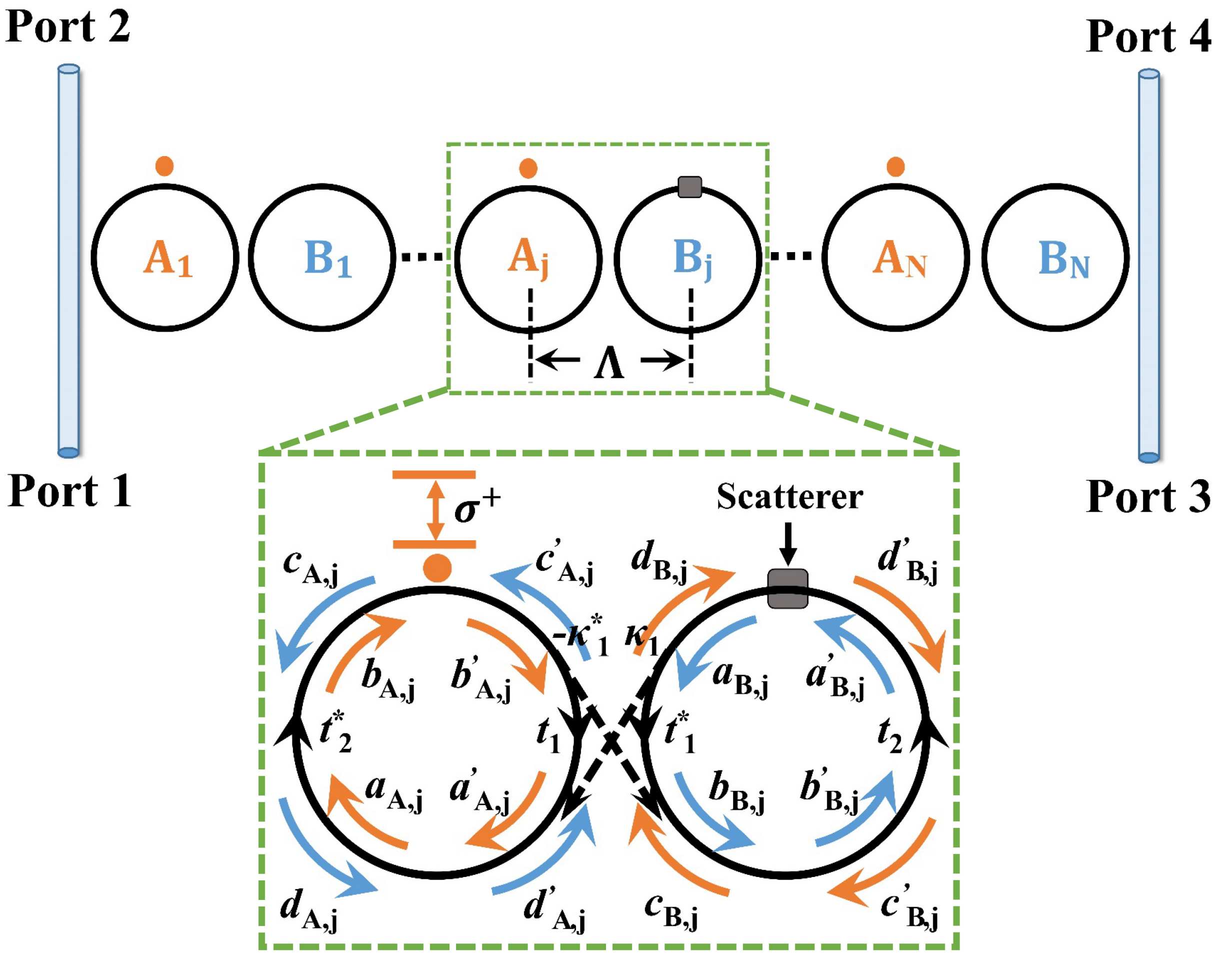

FIG. S5. Schematic of a chiral QE-CROW system containing N unit cells and the input and output waveguides. Inset: we position one scatterer in the middle of the B-sublattice resonator.

In this section, we discuss the effect of the scatterer in our chiral 1D-CROW system shown in Fig. S5. We position one scatterer in the B-sublattice resonator in the middle cell of the CROW. The scatterer will couple the two fields of CW and CCW modes in the B-sublattice resonator. Therefore, the transfer matrix of the scatterer which couples the (a, b) and (c, d) fields together is given by

$$Q_{\text{scatt}} = \frac{1}{t_s} \begin{pmatrix} 1 & 0 & 0 & -r_s \\ 0 & 1 & 0 & 0 \\ 0 & 0 & 1 & 0 \\ r_s & 0 & 0 & 1 \end{pmatrix}, \tag{S33}$$

where t_s and r_s are the transmission and reflection coefficients introduced by the scatterer, respectively. They satisfy $|t_s|^2 + |r_s|^2 = 1$ when the dissipation of the scatterer is neglected [7, 10]. We assume the scatterer to be weak, thus we have

$$t_s = \cos\epsilon \approx 1 - \frac{\epsilon^2}{2}, \quad r_s = i\sin\epsilon \approx i\epsilon, \tag{S34}$$

with $\epsilon \ll 1$. The coupling strength of the backscattering can be derived as $h = \epsilon \times \mathcal{F}$ [7].

The input and output coupling matrices between the resonators and the waveguides, P_{in} and P_{out}, can be written as

$$P_{\text{in}} = \frac{1}{\kappa_{\text{in}}}\begin{pmatrix} -t_{\text{in}} & 1 & 0 & 0 \\ -1 & t_{\text{in}}^* & 0 & 0 \\ 0 & 0 & -t_{\text{in}} & 1 \\ 0 & 0 & -1 & t_{\text{in}}^* \end{pmatrix}, \quad P_{\text{out}} = \frac{1}{\kappa_{\text{out}}}\begin{pmatrix} 1 & -t_{\text{out}} & 0 & 0 \\ t_{\text{out}}^* & -1 & 0 & 0 \\ 0 & 0 & 1 & -t_{\text{out}} \\ 0 & 0 & t_{\text{out}}^* & -1 \end{pmatrix}, \tag{S35}$$

where $\{t_{\text{in}}, t_{\text{out}}, \kappa_{\text{in}}, \kappa_{\text{out}}\}$ are the transmission and coupling coefficients and they satisfy $|t_{\text{in/out}}|^2 + |\kappa_{\text{in/out}}|^2 = 1$.

Without loss of generality, we put the scatterer in the middle of the B-sublattice resonator, see the inset in Fig. S5. Therefore, the transfer matrix of the unit cell is given by:

$$C_{\text{middle}} = P_2 \cdot Q_2\left(\frac{R}{2}\right) \cdot Q_{\text{scatt}} \cdot Q_2\left(\frac{R}{2}\right) \cdot P_1 \cdot Q_1(R) \ . \tag{S36}$$

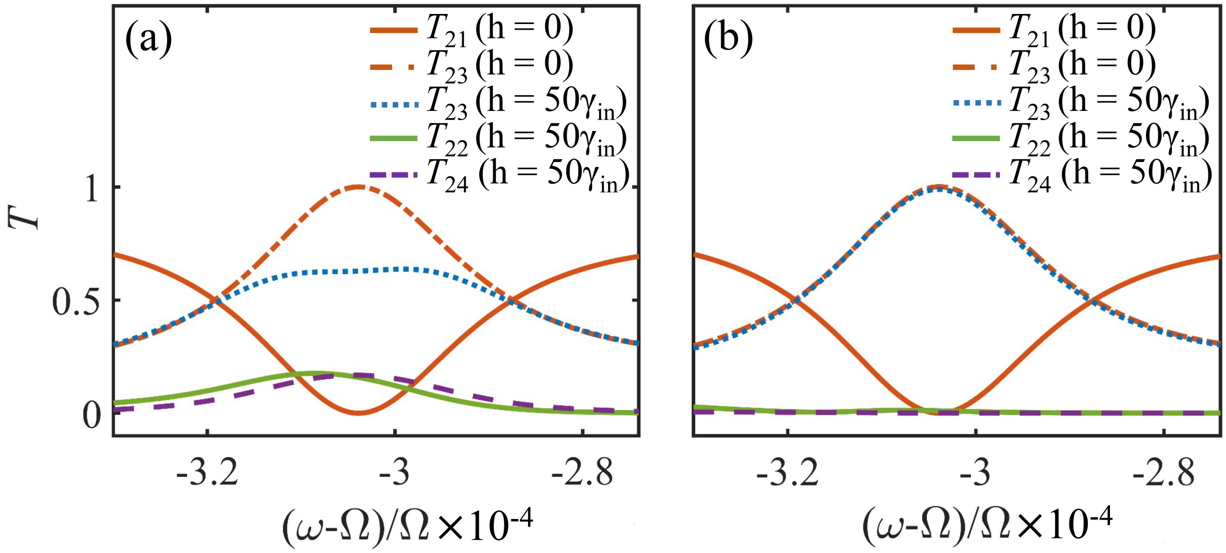

FIG. S6. Robust one-way transmission of the chiral QE-CROW system. Single-photon transmission in the conventional 1D CROW without coupling the QEs (a) and in a chiral QE-CROW system (b). Other parameters are $N = 10$, $\Gamma/\Omega = 1.5 \times 10^{-5}$ ($g/\Omega = 3 \times 10^{-4}$), $\kappa_1 = \kappa_2 = 0.1i$ ($J_1/\Omega = J_2/\Omega = 3 \times 10^{-4}$), $\kappa_{\text{in}} = \kappa_{\text{out}} = 0.25i$, and $\gamma = 0$.

We consider a scatterer embedded in the middle cell of a chiral QE-CROW system, with $N = 10$, $r = 40$ µm, $\Omega/2\pi = 195$ THz, and $n_{\text{eff}} = 2$. The free spectral range of the resonator is calculated as $\mathcal{F}/2\pi = 0.6$ THz. We take $\Gamma/\Omega = 1.5 \times 10^{-5}$, $\kappa_1 = \kappa_2 = 0.1i$, and $\kappa_{\text{in}} = \kappa_{\text{out}} = 0.25i$, so $g/\Omega = 3 \times 10^{-4}$, $J_1/\Omega = J_2/\Omega = 3 \times 10^{-4}$ and the external dissipations of resonators can be calculated as $\gamma_{\text{ex}}/2\pi = 19.4$ GHz [setting $\gamma_{\text{in}} = 0.02\gamma_{\text{ex}}$, thus $\gamma_{\text{tol}}/2\pi = (\gamma_{\text{ex}} + \gamma_{\text{in}})/2\pi = 19.8$ GHz] [7]. These parameter settings are consistent with Fig. 4 in the main text.

The single-photon transmission in our system is robust against backscattering. To justify this, we compare the transmission T_{23} and the backscattering of our chiral QE-CROW system and a conventional CROW system. This scatterer induces a strong backscattering $h = 50\gamma_{\text{in}}$ between the CW and CCW mode in the resonator. The single photon inputs to port 2. In the conventional CROW system equivalent to the case without the QEs, see Fig. S6(a), the scatterer causes a considerable decrease in the transmission T_{23}, reducing it from unity to 0.63. The backscattering also generates a reflection to port 2 and unwanted photon transport to port 4 with equal probability about 18%. In stark contrast, as shown in Fig. S6(b), the scatterer has little influence on photon transmission in our system because the chiral QE-light interaction results in a large frequency splitting $\Delta\Omega$ in the A-sublattice resonator.

VI. THE MAXIMAL ON-SITE DISORDER

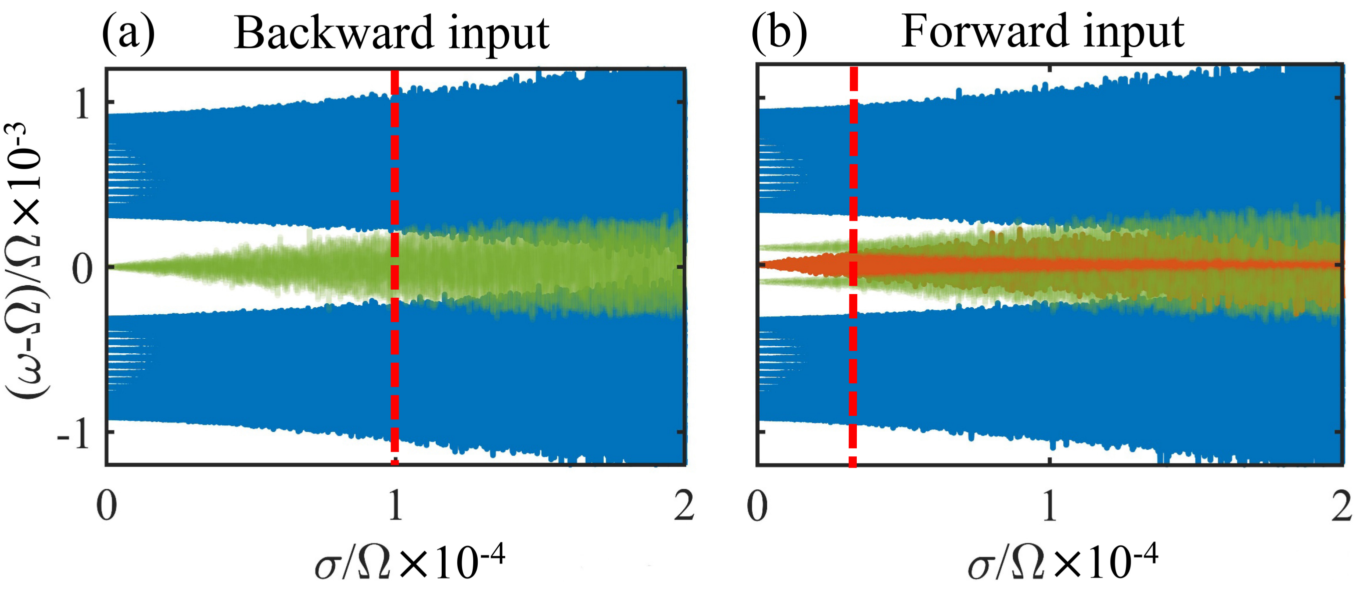

FIG. S7. Band structures versus the disorder strength σ. (a) for the $\mathrm{CCW}_A-\mathrm{CW}_B$ supermode without coupling to the QEs, $g/\Omega=0$. (b) for the $\mathrm{CW}_A-\mathrm{CCW}_B$ supermode with coupling to the QEs, $g/\Omega=1\times10^{-4}$. Other parameters are $N=20$, $J_1/\Omega=3\times10^{-4}$, $J_2=2J_1$.

We now address the effect of the random disorder in the resonance frequency of each resonator. This frequency fluctuation manifests as on-site disorder. The chiral symmetry of the system is broken when considering on-site disorder [11]. The Hamiltonian with a random on-site potential in the rotating frame can be written as

$$\begin{aligned}\hat{H}_{\mathrm{CW}_A-\mathrm{CCW}_B}=&\sum_{j}^{N}\left(\epsilon_{a,j}\hat{a}^{\dagger}_{j,\circlearrowright}\hat{a}_{j,\circlearrowright}+\epsilon_{b,j}\hat{b}^{\dagger}_{j,\circlearrowleft}\hat{b}_{j,\circlearrowleft}\right)\\&+\sum_{j}^{N}\left(g\hat{a}^{\dagger}_{j,\circlearrowright}\hat{\sigma}_j+J_1\hat{a}^{\dagger}_{j,\circlearrowright}\hat{b}_{j,\circlearrowleft}+\mathrm{H.c.}\right)+\sum_{j}^{N-1}\left(J_2\hat{a}^{\dagger}_{j+1,\circlearrowright}\hat{b}_{j,\circlearrowleft}+\mathrm{H.c.}\right)\end{aligned}\tag{S37}$$

for the forward-input case and

$$\begin{aligned}\hat{H}_{\mathrm{CCW}_A-\mathrm{CW}_B}=&\sum_{j}^{N}\left(\epsilon_{a,j}\hat{a}^{\dagger}_{j,\circlearrowleft}\hat{a}_{j,\circlearrowleft}+\epsilon_{b,j}\hat{b}^{\dagger}_{j,\circlearrowright}\hat{b}_{j,\circlearrowright}\right)\\&+\sum_{j}^{N}\left(J_1\hat{a}^{\dagger}_{j,\circlearrowleft}\hat{b}_{j,\circlearrowright}+\mathrm{H.c.}\right)+\sum_{j}^{N-1}\left(J_2\hat{a}^{\dagger}_{j+1,\circlearrowleft}\hat{b}_{j,\circlearrowright}+\mathrm{H.c.}\right)\end{aligned}\tag{S38}$$

for the backward-input case. Here, $\epsilon_{a,j}$ $(\epsilon_{b,j})$ is a random variable that obeys a Gaussian distribution with a mean of zero and a standard deviation σ. We define the standard deviation σ as the disorder strength. By diagonalizing Eqs. (S37) and (S38) for $N=20$ unit cells, we show the band structures as a function of the disorder strength σ in the case of $J_2=2J_1$, see Fig. S7. The fluctuation of the resonator frequency leads to the diffusion of each band. As a result, with the increase of the disorder strength, the edge-state spectra gradually overlap with the bulk-state spectra, see Fig. S7. We evaluate the maximum on-site disorder when the edge-state and the bulk-state bands begin to overlap. For the backward-input case, the band of edge state overlaps with the upper and lower bulk bands at about $\sigma/\Omega=1\times10^{-4}$. Therefore, the maximal on-site disorder is $\sigma_{\max}/\Omega=1\times10^{-4}$ [see the red dashed line in Fig. S7(a)]. Figure S7(b) corresponds ot the forward-input case. In this case, the maximal disorder is about $\sigma_{\max}/\Omega=0.4\times10^{-4}$ when $g/\Omega=1\times10^{-4}$.

Figure S8 shows the maximal disorder $\sigma_{\max}$ as a function of g in the forward-input case. When the coupling strength g is small, $\sigma_{\max}$ is limited by the flat-band diffusion. The maximal disorder increases with the increasing g due to

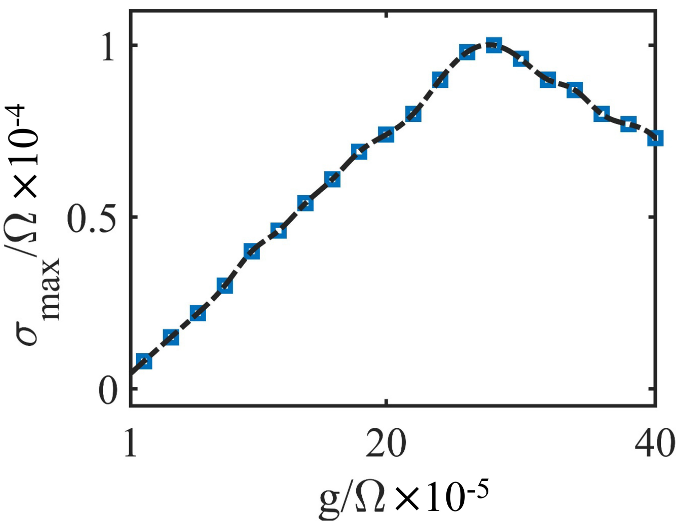

FIG. S8. The maximal disorder versus the coupling strength g in the forward-input case. Other parameters: $N = 20$, $J_1/\Omega = 3 \times 10^{-4}$, $J_2 = 2J_1$.

the splitting of the edge-state eigenenergies with respect to the zero energy, see Fig. 2(c) in the main text. It reaches a maximum at $g/\Omega = 2.8 \times 10^{-4}$, about $\sigma_{\max}/\Omega = 1 \times 10^{-4}$, when the edge-state bands first overlap with the upper and lower bulk bands. After that, the maximal disorder gradually decreases due to the limitation of the diffusion of bulk bands.

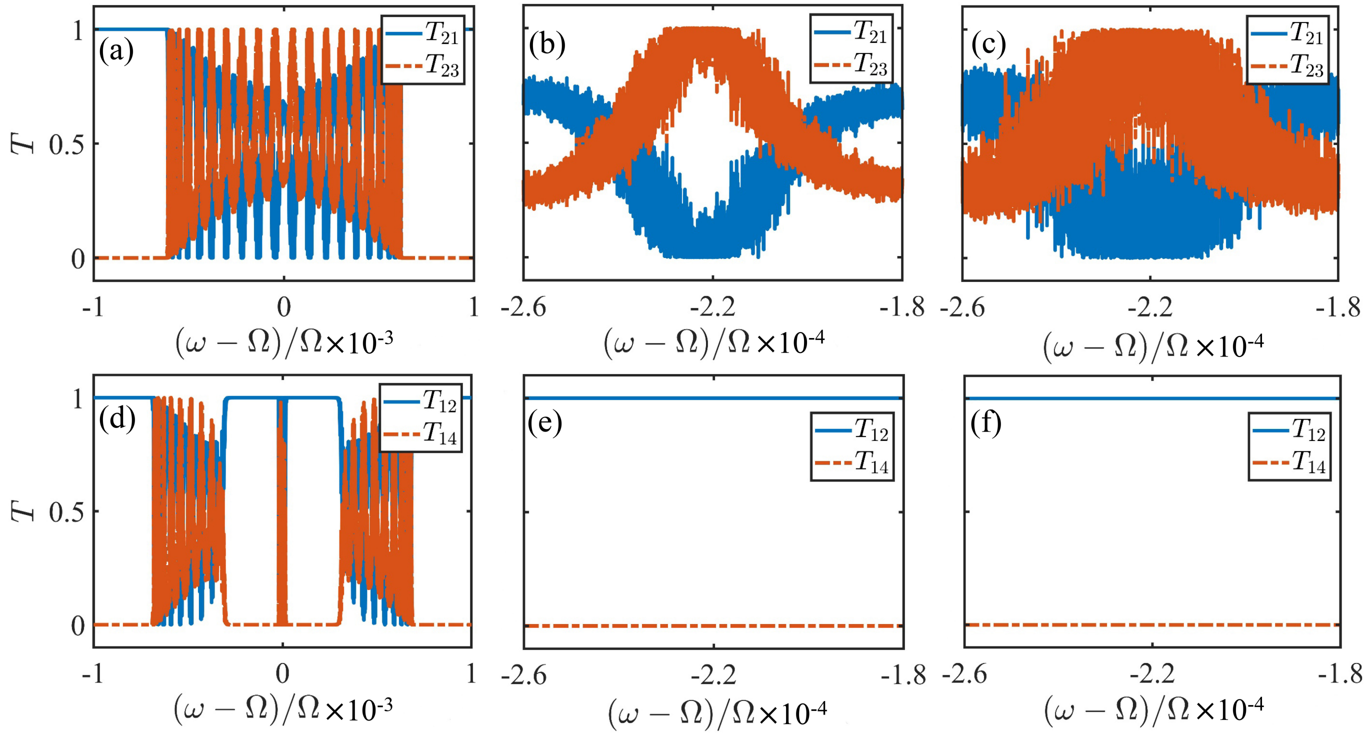

FIG. S9. Influence of the on-site disorder on transmission spectra. In (a-c) the $\mathrm{CCW}_A - \mathrm{CW}_B$ supermode is driven, where $g = 0$, $\sigma/\Omega = 1 \times 10^{-5}$ for (a, b), and $\sigma/\Omega = 2 \times 10^{-5}$ for (c). In (d-f) the $\mathrm{CW}_A - \mathrm{CCW}_B$ is excited, where $g/\Omega = 3 \times 10^{-4}$, $\sigma/\Omega = 1 \times 10^{-5}$ for (d, e), and $\sigma/\Omega = 2 \times 10^{-5}$ for (e). Other parameters are $N = 10$, $J_1/\Omega = 3 \times 10^{-4}$, $J_2 = J_1$, and $\kappa_{\text{in}} = \kappa_{\text{out}} = 0.25i$.

Next, we study the effect of the on-site disorder on the transmission spectra in the case of $J_1 = J_2$. By introducing random disorders to each resonator frequency in the transfer matrix, that is $\tilde{\Omega}_j$ for the jth resonator, we can evaluate the influence of the on-site disorder as shown in Fig. S9. The random variable $\tilde{\Omega}_j$ follows a Gaussian distribution, with a mean of Ω and a standard deviation of σ. For the backward input, the on-site disorder, with a strength $\sigma/\Omega = 1 \times 10^{-5}$, causes fluctuations in the transmission spectra, see Fig. S9(a) and Fig. S9(b) zoomed in a specific single-frequency window. A maximum allowable disorder, about $\sigma_{\max}/\Omega = 2 \times 10^{-5}$, corresponds to the complete indistinguishability of transmissions T_{21} and T_{23}. In contrast, in the case of forward input, working in the nonreciprocal band gap, the transmission spectra are hardly affected by the on-site order, see Fig. S9(d-f). The band gap protects the transmission spectra from the on-site disorder. Therefore, a high performance of the frequency-multiplexed single-photon circulator can also be obtained even in a large on-site disorder. Note that similar results can also be obtained for the on-site disorder subject to uniform distribution.

VII. INFLUENCE OF THE NUMBER OF UNIT CELLS

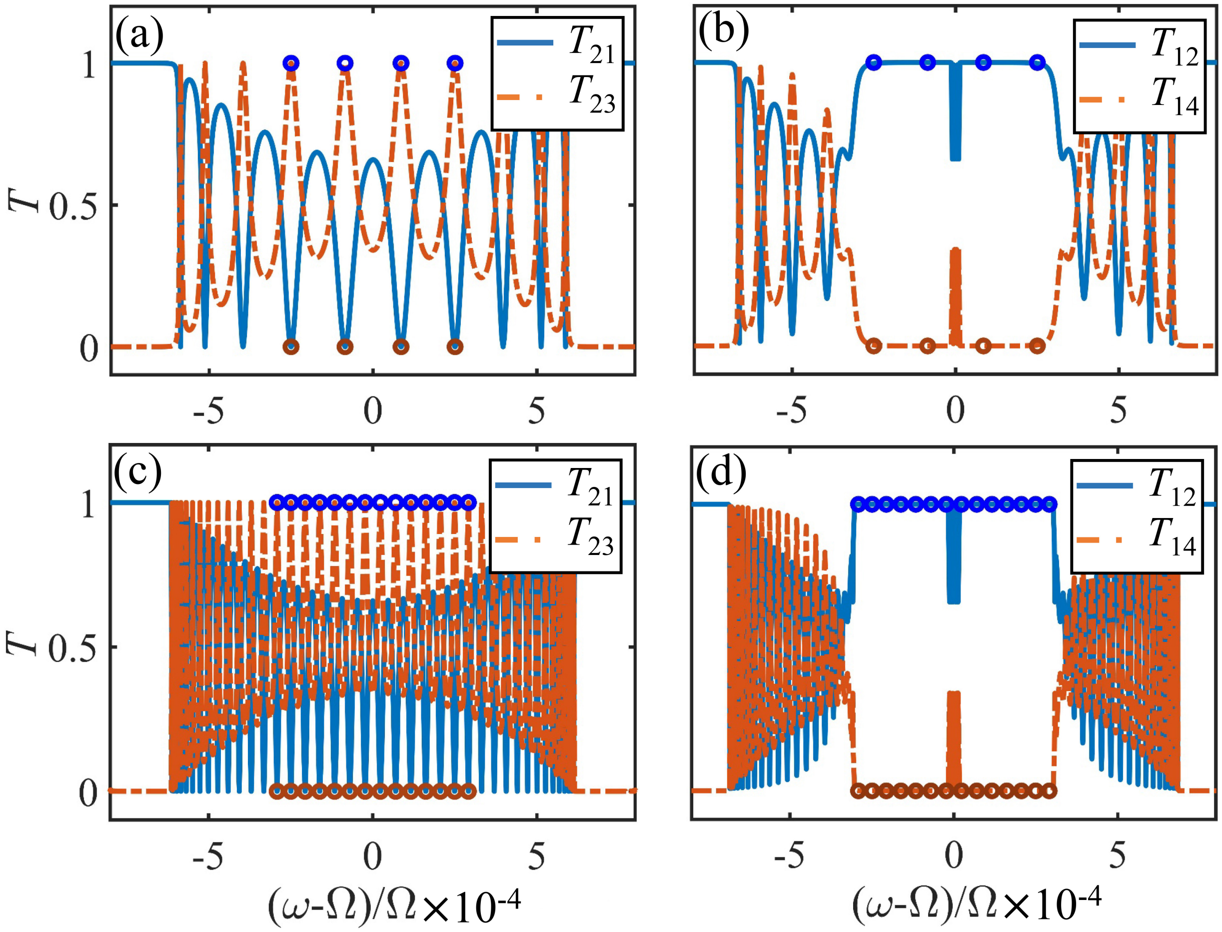

FIG. S10. Transmission of the chiral QE-CROW system with $N = 5$ in (a) and (b) and $N = 20$ in (c) and (d). In (a) and (c) the single photon incidents to port 2. In (b) and (d) the single photon incidents port 1 with $\Gamma/\Omega = 1.5 \times 10^{-5}$. Other parameter are $\gamma = 0$, $\kappa_{\text{in}} = \kappa_{\text{out}} = 0.25i$, and $\kappa_1 = \kappa_2 = 0.1i$.

In this section, we study the effect of the number of unit cells N on the frequency-multiplexed channels of the single-photon circulator.

On the one hand, as we discussed in the main text, when the single photon is incident into the port 2, the excited $\text{CCW}_A - \text{CW}_B$ modes decouple from the QEs. In this case, the number of transmitted peaks and dips formed is proportional to $2N$, see Figs. S10(a) and (c) for $N = 5$ and $N = 20$, respectively.

On the other hand, the bandwidth of the edge state formed by the input in the opposite direction, i.e., the port 1, depends only on the QE-resonator coupling strength g, and does not depend on the number of unit cells. Therefore, at a given decay rate Γ for determining the QE-resonator coupling strength by $g \approx \sqrt{2\Gamma \times \mathcal{F}}$, we can increase and adjust the frequency-multiplexed channels of the single-photon circulator by increasing the number of cells N. For example, there are 4 and 14 nonreciprocal windows for $N = 5$ and $N = 20$ with $\Gamma/\Omega = 1.5 \times 10^{-5}$, see the blue dots in Figs. S10(b) and (c), respectively.

VIII. FIRST-PRINCIPLE ANALYSIS USING FDTD METHOD

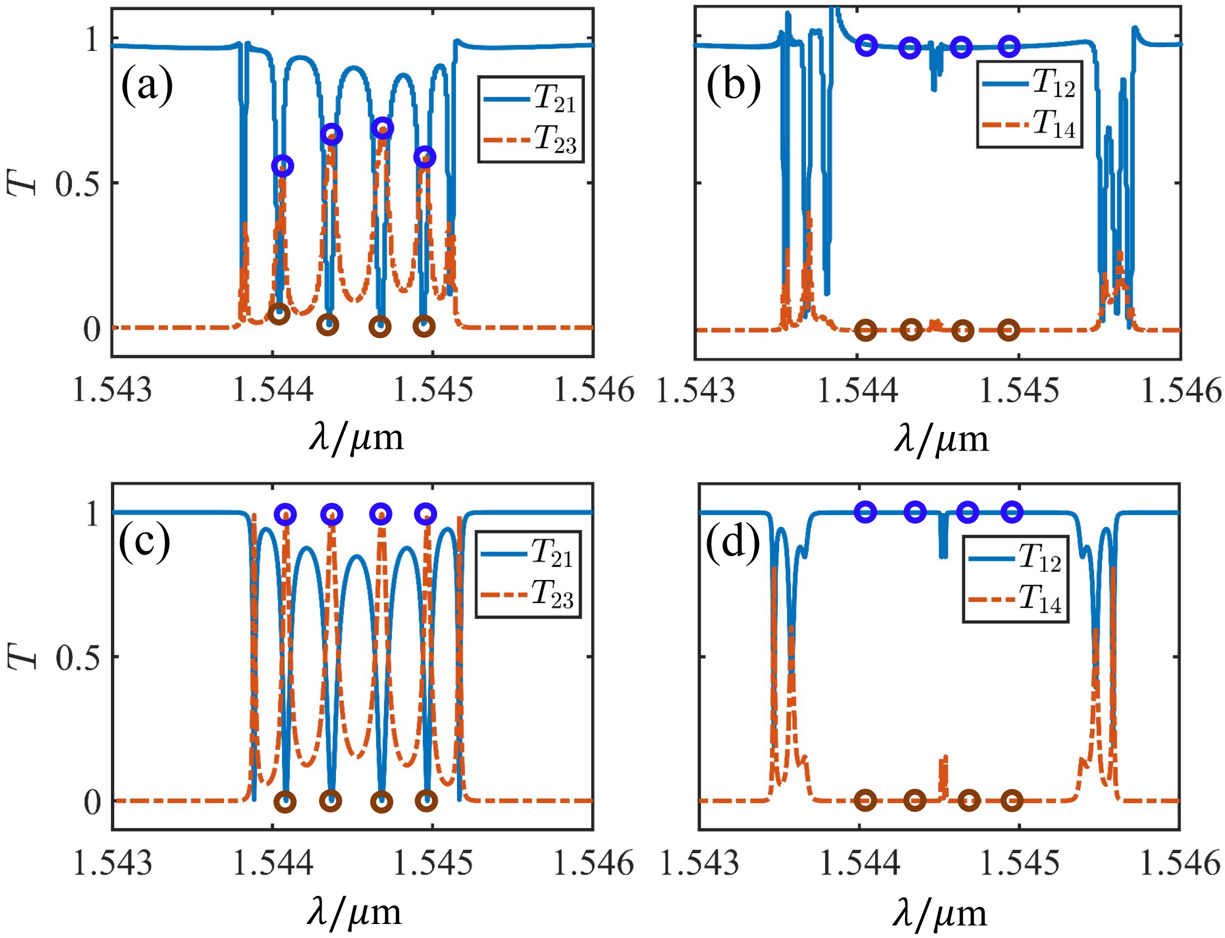

FIG. S11. Transmission of the chiral QE-CROW system using $N = 3$. (a) and (b) are the results of our simulation using FDTD method. (c) and (d) are calculated by the transfer matrix method. In (a, c) the $\mathrm{CCW}_A - \mathrm{CW}_B$ supermode is driven. In (b, d), the $\mathrm{CW}_A - \mathrm{CCW}_B$ is excited.

It is an open question to analyze the interaction between resonators and QEs from the first-principle analysis, especially in quantum regime. Here, we show an equivalent numerical method using finite-difference time-domain (FDTD) to simulate the propagation of a single photon in our chiral QE-CROW system. To simulate the chiral interaction between the QEs and resonators, we divide the system into two parts, the forward-input and the backward-input cases, and analyze them separately.

In the backward-input case, the system reduces to a classical CROW due to the decoupling of the QEs with the A-sublattice resonators. We can simulate the transport of single photons in this system with the FDTD slover of the Lumerical software. For the sake of computational resources and time, we set the number of the unit cells to be $N = 3$ and the radius of each microring resonator to be $r = 4$ μm, to display a physical picture. We use silicon, with a refractive index $n_{\mathrm{eff}} = 3.48$, to simulate microring resonators and waveguides. The microring resonators and waveguides are 0.45 μm wide and 0.22 μm thick. Through the numerical simulation with FDTD method, we obtain an intrinsic quality factor of $Q_{\mathrm{in}} \approx 1 \times 10^5$ at the wavelength $\lambda_r \sim 1.546$ μm, and a mode volume $V_{\mathrm{m}} \sim 1.67$ μm^3. The corresponding resonance frequency and the intrinsic decay rate of microring resonators are $\Omega/2\pi \approx 194.11$ THz and $\gamma_{\mathrm{in}}/2\pi \approx 1.9$ GHz, respectively. The relatively low quality factor of microring resonators is due to the large spatial grid in the simulation, limited by available computational resources. The gap between the waveguide and microring resonators is set to 0.13 μm. The spacing between the A-sublattice and B-sublattice resonators is 0.2 μm. The input light is exclusively transversally polarized. As a result, the evanescent filed of each microring resonator is almost perfectly circularly polarized with its polarization locked to the propagating direction [12–14].

In the forward-input case, the QEs are coupled to the resonators and the system becomes an L-shaped chain. In the single-excitation space we are interested in, Fock state of an optical cavity can be truncated up to $|1\rangle$, which is equivalent to a two-level QE [15]. Therefore, we can use a side-coupled microring resonator to model the two-level QE when we consider the transport of single photons. In this treatment, a microring resonator supporting the directional-circulating whispering-gallery mode is equivalent to the two-level QE chirally interacting with the A-sublattice resonator [16]. Thus, by setting the side-coupled resonators with the same resonance frequency as the QEs, we can use the FDTD method to numerically simulate the transport of a single photon in the case of forward input. The gap between the A-sublattice resonator and the side-coupled resonator is set to 0.1 μm. Other parameters in the FDTD simulation are the same as those in backward-input case.

Now, we numerically evaluate the performance of our frequency-multiplexed single-photon circulator. As expected, the results of the FDTD simulation show a nonreciprocal transmission spectra, see Figs. S11(a) and S11(b). For the backward input, the system is excited in the $\mathrm{CCW}_A - \mathrm{CW}_B$ supermode. Taking the input to port 2 as an example, there are six peaks in the transmission T_{23} and six dips in T_{21}, as shown in Fig. S11(a). Two reasons cause the loss of the transmission T_{23}: one is the intrinsic decay of microring resonators, such as the large bending losses for such small-radius microring resonators; the other is that the backscattering caused by the large grid of differential space in the FDTD simulation. By further decreasing the spatial grid in the simulation and correspondingly increasing the computation resources, we can eliminate the backscattering, and thus improve the transmission T_{23}.

For the forward input, we take the light to be incident from port 1. Because of the large computational complexity, the simulation time will be very long, if we want to obtain a smooth transmission below unity. As a result, some values of the transmission T_{12} exceed 1, see the blue solid curve in Fig. S11(b). These abnormal values can disappear when the simulation time is long enough. Considering the symmetry of the CROW, we have $T_{12} = T_{34}$ and $T_{23} = T_{41}$. Thus, we can obtain a frequency-multiplexed single-photon circulator with four optimized frequency windows at $\omega/2\pi \approx \{194.16, 194.12, 194.08, 194.04\}$ THz. The circling photon transport direction is $1 \to 2 \to 3 \to 4 \to 1$. The corresponding fidelity and average photon survival probability of the circulator are calculated as $\{0.96, 0.99, 0.99, 0.99\}$ and $\{0.79, 0.82, 0.83, 0.79\}$, respectively. The average insertion loss for these four frequency windows is about 1.12 dB. Note that the simulated single-photon survival probability is smaller than the real value. By reducing the spatial grid in the simulation to eliminate the backscattering, we can get more accurate single-photon survival probability.

The results calculated by the transfer matrix method agree well with the simulation results, see Figs. S11(c) and S11(d). We take $\kappa_{\mathrm{in}} = \kappa_{\mathrm{out}} = 0.2i$, $\kappa_1 = \kappa_2 = 0.1i$, $\gamma_{\mathrm{in}}/2\pi = 25$ GHz, and $g/\Omega = 1.5 \times 10^{-3}$. A higher transmission T_{23}, corresponding to the case without the differential-induced backscattering, can be obtained as shown in Fig. S11(c). Therefore, we can actually get a better performance frequency-multiplexed single-photon circulator.

We also demonstrate how our single-photon circulator works by simulating the steady-state distribution of the magnetic field H component of the incident light field, see Fig. S12. When a single photon is incident to port 2 at the transmission peak indicated by the open circles in Fig. S11, it exits from port 3. The small amount of light field escaping from port 4 originates from the differential-induced backscattering. It can be eliminated by decreasing the spatial grid in the FDTD simulation. In contrast, due to the nonreciprocal band gap, the photon incident from port 1 exits totally from port 2. According to the symmetry of the CROW, the photon incident from port 3 (port 4) will be emitted from port 4 (port 1). Therefore, our chiral QE-CROW system promises a perfect frequency-multiplexed single-photon circulator.

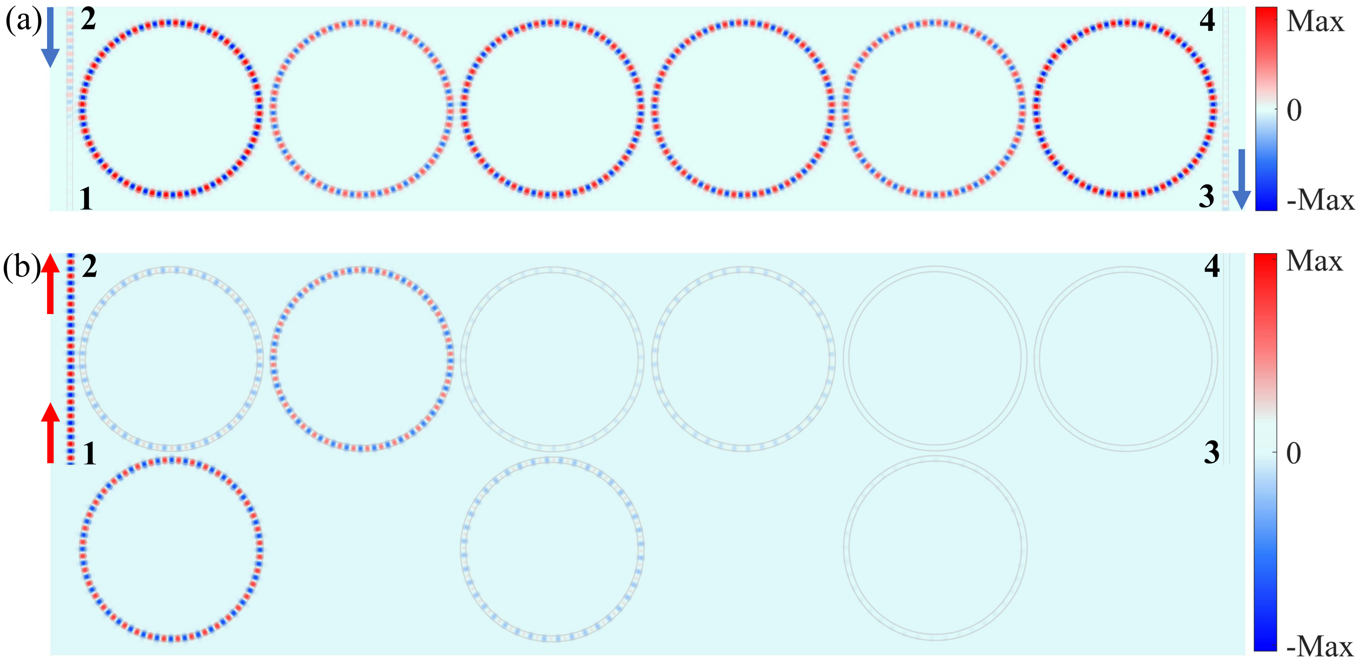

FIG. S12. Distribution of the magnetic component H of the light field in the backward-input case (a) and in the forward-input case (b). The frequency chosen in our simulation is $\omega/2\pi = 194.12$ THz ($\lambda/\mu\text{m} = 1.5444$). Other parameters are the same as Fig. S11. Note that the field in the resonators in (a) is stronger than that in the waveguide because of the effect of resonator enhancement.

[1] Y. Peng, Y. Bao, and F. von Oppen, Boundary Green functions of topological insulators and superconductors, Phys. Rev. B **95**, 235143 (2017).

[2] V. M. Martinez Alvarez and M. D. Coutinho-Filho, Edge states in trimer lattices, Phys. Rev. A **99**, 013833 (2019).

[3] J. K. Asbóth, L. Oroszlány, and A. Pályi, A short course on topological insulators: Band-structure and edge states in one and two dimensions, Lecture notes in physics **919**, 166 (2016).

[4] M. Kremer, I. Petrides, E. Meyer, M. Heinrich, O. Zilberberg, and A. Szameit, A square-root topological insulator with non-quantized indices realized with photonic Aharonov-Bohm cages, Nat. Commun. **11**, 907 (2020).

[5] A. Anastasiadis, G. Styliaris, R. Chaunsali, G. Theocharis, and F. K. Diakonos, Bulk-edge correspondence in the trimer Su-Schrieffer-Heeger model, arXiv preprint arXiv:2202.13789 (2022).

[6] G. Cáceres-Aravena, B. Real, D. Guzmán-Silva, A. Amo, L. E. F. Foa Torres, and R. A. Vicencio, Experimental observation of edge states in SSH-Stub photonic lattices, Phys. Rev. Research **4**, 013185 (2022).

[7] J. Tang, L. Tang, and K. Xia, Single-photon transport in a whispering-gallery mode microresonator directionally coupled with a two-level quantum emitter, arXiv preprint arXiv:2110.09375 (2021).

[8] K. Xia, G. Lu, G. Lin, Y. Cheng, Y. Niu, S. Gong, and J. Twamley, Reversible nonmagnetic single-photon isolation using unbalanced quantum coupling, Phys. Rev. A **90**, 043802 (2014).

[9] J. K. S. Poon, J. Scheuer, S. Mookherjea, G. T. Paloczi, Y. Huang, and A. Yariv, Matrix analysis of microring coupled-resonator optical waveguides, Opt. Express **12**, 90 (2004).

[10] M. Hafezi, E. A. Demler, M. D. Lukin, and J. M. Taylor, Robust optical delay lines with topological protection, Nat. Phys. **7**, 907 (2011).

[11] M. Scollon and M. P. Kennett, Persistence of chirality in the Su-Schrieffer-Heeger model in the presence of on-site disorder, Phys. Rev. B **101**, 144204 (2020).

[12] K. Y. Bliokh, D. Smirnova, and F. Nori, Quantum spin Hall effect of light, Science **348**, 1448 (2015).

[13] F. Alpeggiani, K. Y. Bliokh, F. Nori, and L. Kuipers, Electromagnetic Helicity in Complex Media, Phys. Rev. Lett. **120**, 243605 (2018).

[14] L. Tang, J. Tang, W. Zhang, G. Lu, H. Zhang, Y. Zhang, K. Xia, and M. Xiao, On-chip chiral single-photon interface: Isolation and unidirectional emission, Phys. Rev. A **99**, 043833 (2019).

[15] D. F. Walls and G. J. Milburn, *Quantum optics*, 2nd ed. (Springer Science & Business Media, Berlin, Germany, 2007).

[16] J.-T. Shen and S. Fan, Theory of single-photon transport in a single-mode waveguide. I. Coupling to a cavity containing a two-level atom, Phys. Rev. A **79**, 023837 (2009).